Nano Today 52 (2023) 101958

Contents lists available at ScienceDirect

Nano Today

journal homepage: www.elsevier.com/locate/nanotoday

Facile design of multifunctional melamine foam with Ni-anchored reduced graphene oxide/MXene as highly efficient microwave absorber

Haoran Cheng [a,b,1], Yamin Pan [a,1], Wei Li [c], Chuntai Liu [a], Changyu Shen [a], Xianhu Liu [a,*], Caofen Pan [b,*]

[a] College of Materials Science and Engineering, State Key Laboratory of Structural Analysis, Optimization and CAE Software for Industrial Equipment, National Engineering Research Center for Advanced Polymer Processing Technology, Zhengzhou University, Zhengzhou 450002, China
[b] CAS Center for Excellence in Nanoscience, Beijing Institute of Nanoenergy and Nanosystems, Chinese Academy of Sciences, Beijing 101400, China
[c] Department of Materials and Earth Sciences, Technical University of Darmstadt, 64287 Darmstadt, Germany

ARTICLE INFO

Keywords:
Graphene
$Ti_3C_2T_x$ MXene
Microwave absorption
Multifunction

ABSTRACT

The appropriate multi-component strategies and ingenious microstructure design remain challenging for the development of multifunctional and high-performance electromagnetic wave absorbing materials. Here, magnetic Ni nanoparticles-anchored reduced graphene oxide (RGO)/$Ti_3C_2T_x$ MXene hybrids were successfully assembled on melamine foam (MF) via electrostatic self-assembly and hydrazine vapor reduction processes, achieving high-performance electromagnetic wave absorption and multifunctionality. Interestingly, the RGO/MXene/Ni-MF achieves high-performance microwave absorption with a minimum reflection loss value of − 61.3 dB and a maximum width effective absorption bandwidth (EAB) of 7.04 GHz. The superior electromagnetic wave absorption stems from a 3D dielectric/magnetic network with satisfactory impedance matching, dielectric/magnetic losses, interface/dipole polarization and multiple reflection scattering. Furthermore, the RGO/MXene/Ni-MF also revealed outstanding hydrophobicity, thermal insulation, infrared shielding and incombustibility. This work opens up novel prospects for developing lightweight, multifunctional microwave absorbers for practical applications.

Introduction

To overcome the ubiquitous and increasingly serious problems of electromagnetic interference and pollution, more and more researchers are developing advanced electromagnetic wave (EMW) absorbing materials with excellent absorption performances of lightweight, thin matching thickness, strong absorption and broad bandwidth[1–4]. Generally, EMW absorption performances are closely related to the multi-component, microstructure and electromagnetic mechanisms of materials[5,6]. Therefore, multi-component hybrid materials with ingenious structural designs will become the research focus of future high-performance microwave absorbing materials.

So far, in the family of EMW absorbing materials, the two-dimensional materials graphene [7], MXene [8] and MoS_2 [9] are considered the most potential candidates. Among them, graphene oxide material has attracted extensive attention in EMW absorption due to its various remarkable properties such as low density, high specific surface area, large aspect ratio, and high-temperature stability [10–12]. However, a single GO material has problems such as improper electrical conductivity leading to impedance mismatch and limited loss mechanism. Therefore, the addition of other lossy materials has been widely used as a necessary solution to improve its microwave absorption performance. Recently, MXene with unique structural and electronic properties has shown great promise in EMW absorption applications, its outstanding conductivity and rich surface groups could provide strong conduction loss and polarization loss [13–15], which can make up for its loss limitation after combining with GO. The outstanding chemical/physical performances and structures enable RGO/MXene-based hybrids hopeful candidates for the preparation of wideband EMW absorbing materials [16,17]. For example, Yin et al. synthesized the hollow core-shell RGO/MXene foam exhibit an RL_{min} of − 23 dB with EAB occupying the X-band [18]. However, the sole permittivity loss scheme of RGO/MXene hybrids, and the impedance mismatch due to the tightly interconnected electronic transport networks, limit the further

* Corresponding authors.
E-mail addresses: xianhu.liu@zzu.edu.cn (X. Liu), cfpan@binn.cas.cn (C. Pan).
[1] These authors contributed equally to this work

https://doi.org/10.1016/j.nantod.2023.101958
Received 20 February 2023; Received in revised form 27 April 2023; Accepted 5 August 2023
Available online 15 August 2023

enhancement of the strong absorption performances. Based on the synergistic electromagnetic loss effect of dielectric/magnetic composites, magnetic components were coupled with RGO/MXene hybrids to enrich the loss mechanism and enhance impedance matching [19]. For instance, Che et al. fabricated the MXene-rGO/CoNi film exhibiting excellent microwave absorption properties with the RL_{min} − 54.1 dB at 13.28 GHz [20].

It is well known that ingenious structural design can effectively dissipate EMW, such as petal-like [21], hollow [22], core-shell [23] and 3D porous structures [24]. Wang et al. synthesized a MOF derivative/MXene hybrid with a petal-like structure, achieving the optimal RL_{min} of − 58.37 dB [25]. Che et al. obtained core-shell structured 3D MXene@Ni microspheres with RL_{min} of − 59.3 dB [26]. Liu et al. constructed 3D porous M_OS_2/MXene aerogels with the conformal heterogeneous interface, exhibiting RL_{min} of − 61.65 dB [27]. Lu et al. fabricated a highly cross-linked 3D-structured Fe/Fe_2O_3 @porous carbon composite, the RL_{min} and EAB reach − 54.7 dB and 6.4 GHz, respectively [28]. Qiu et al. constructed a dual-3D continuous-phase structured $Co_{1.29}Ni_{1.71}O_4$/RGO/CF syntactic foam with a RL_{min} of − 53.45 dB at 3.0 mm thickness and an EAB of 7.45 GHz [29]. Ji et al. synthesized a hybrid melamine foam (MF) of 3D porous structure, achieving a RL_{min} of − 59.8 dB and a maximum EAB of 5.64 GHz [30]. The above results show that the structural design of the absorber could effectively influence the absorbing property by adjusting the interface polarization. In particular, the 3D interconnected porous structure of MF endows the absorber with the benefits of lightweight, rich interfacial/dipole polarization, multiple scattering and reflections due to its abundant pores and high specific surface area, thereby attenuating more EMW [31,32]. Therefore, the combination of multi-component RGO/MXene/Ni hybrid with 3D interconnected porous structure can enhance the complex permittivity, improve impedance matching, offer the rich interface and dipole polarization, and extend the transmission path of EMW, thereby increasing multiple scattering and reflection, which was considered to be an effective way to realize outstanding EMW absorption performance.

In addition, to meet the demands of an increasingly diverse environment, sophisticated absorbers also require various functions such as hydrophobicity, heat insulation and flame retardancy [33–35]. For instance, absorbers with hydrophobicity can maintain excellent durability and stability in wet or water environments [36]. The excellent thermal insulation properties and flame retardancy could protect sensitive flammable units from high-temperature attack or burn damage and are necessary for military equipment to realize both radar stealth and infrared stealth [37]. However, to our knowledge, it is stills a huge challenge to integrate high-performance microwave absorption and multifunctional properties.

Herein, we successfully synthesized Ni^{2+} anchored GO/MXene hybrids via hydrogen bonding and electrostatic self-assembly. Then, RGO/MXene/Ni (RMNi) was assembled on the MF surface by impregnation method and mild hydrazine vapor reduction, realizing high-performance microwave absorption and versatility. Owing to the synergistic effect of dielectric and magnetic losses, suitable impedance matching, abundant interfacial/dipole polarization, multiple reflections and scattering, suitable reduction and N atom doping modification, RMNi-MF achieve high microwave absorption performance with ultra-low RL_{min} of − 61.3 dB and maximum EAB of 7.04 GHz, covering the entire Ku-band. Besides, the excellent hydrophobicity, thermal insulation, flame retardancy and infrared shielding function combined with the excellent EMW absorption ability endow the RMNi-MF composite with great application prospects in various complex environments.

Results and discussion

Fig. 1a describes the preparation process of RMNi-MF. First, GO with strong gelation ability was introduced into MXene suspensions as chemical linkers, and stable GO/MXene suspensions were easily formed due to their similar hydrophilicity and negative zeta potential [38]. Second, the GO/MXene hybrid can adsorb the introduced Ni^{2+} ions to the surface through electrostatic self-assembly induced by opposite surface charges, and provide uniform and efficient nucleation sites for the growth of Ni magnetic nanoparticles [39]. Among them, the $Ni(OH)_2$ precursor was formed by the complexation of attached Ni^{2+} ions and OH- ions under alkaline conditions. Subsequently, the PDA-modified MF was immersed in the $RMNi^{2+}$ solution, thanks to the strong capillary force of MF and the adhesion of PDA, $RMNi^{2+}$ was firmly assembled on the surface of MF. Finally, RMNi-MF was obtained by reduction/modification under ethylene glycol and moderate hydrazine steam treatment. Among them, GO/MXene was weakly reduced and nitrogen-doped, and Ni^{2+} ions are reduced as Ni magnetic nanoparticles anchored on the surface of RGO/MXene, which can help to improve the electron transport in the conductive pathway and enrich the polarized groups.

The structural evolution and surface chemistry are the keys to achieving excellent EMW absorption properties and specific multifunctionality. The existence of RGO, MXene and Ni magnetic nanoparticles in the RMNi hybrid was confirmed by comparing the XRD patterns (Fig. 1b). The (002) diffraction peak of RMNi at 6.3° indicates that the structure of MXene sheets is well preserved after electrostatic self-assembly, and the increase of layer spacing is due to the intercalated RGO sheets and the in-situ growth of Ni magnetic nanoparticles. The presence of RGO is reflected in a broad and weak peak at 24.3°, which is attributed to hydrazine vapor-reduced GO. The diffraction peaks at 44.6, 51.9 and 76.8° correspond perfectly to the face-centered cubic (111), (200) and (220) planes of Ni (PDF#03–1051) [40,41], further confirming the successful preparation of RMNi hybrids. In addition, the Raman spectra of GO, RGO, RM and RMNi were compared, and the D and G peaks located at 1345 cm^{-1} and 1597 cm^{-1}, respectively, correlate with the presence of the graphene lattice (Fig. 1d). Among them, the I_D/I_G of RMNi, RM and RGO were all larger than that of GO, which further confirmed that the restoration of the conjugate region on RGO via the hydrazine vapor.

The XPS was used to analyze the chemical structure and elemental composition of the hybrid. The results show the newly added N 1s peak in the RMNi hybrid after reduced/modified, indicating successful doping modification of N atoms (Fig. 1e). The doped N atoms exist on graphene and MXene as pyridine-N (399.1 eV), pyrrole-N (400.2 eV) and graphitic-N (401.3 eV), respectively (Fig. 1f), which could effectively decrease the intrinsic resistance and enhance their electron transport capacity [42,43]. In addition, the C-N bond in C1s further demonstrated the doping modification of the hybrid by hydrazine vapor (Fig. 1g). On the other hand, the reduction of C/O in RMNi and the decay of oxygen-containing group bonds demonstrate the efficient reduction and modification of GO and MXene via hydrazine vapor (Fig. 1h). Among them, the modified removal of polar groups (eg, -F, -OH, and -COOH) play a significant role in the excellent hydrophobicity [44,45].

The Ti 2p related four peaks of RMNi hybrids at 465.2, 461.9, 459.4, and 456.1 eV correspond to Ti-O $2p_{1/2}$, C-Ti-T_x $2p_{1/2}$, Ti-O $2p_{3/2}$, and C-Ti-T_x $2p_{3/2}$ bonds (Fig. 1i) [46]. While the main peaks of Ni 2p spectrum at 873.9 eV and 855.8 eV correspond to Ni 2p1/2 and Ni 2p3/2 (Fig. 1j), respectively, indicating the successful introduction of Ni magnetic nanoparticles [47]. In addition, in the FT-IR spectra, the newly added N–H bond and C–N bond and the weakening of oxygen-containing groups also demonstrate the reduction/modification process (Fig. 1c). These abundant functional groups and doped N atoms can interact with EMW to induce dipole polarization and defect polarization, thus improving EMW absorption [48,49].

The microstructure of composite foams was determined using atomic force microscopy (AFM), transmission electron microscopy (TEM) and scanning electron microscopy (SEM). The as-prepared monolayer GO with a lateral dimension of about 2.1 μm and a thickness of about 1.9 nm (Fig. 2a); the as-synthesized $Ti_3C_2T_x$ MXene nanosheet has a lateral dimension of about 0.9 μm and a typical thickness of about 1.1 nm

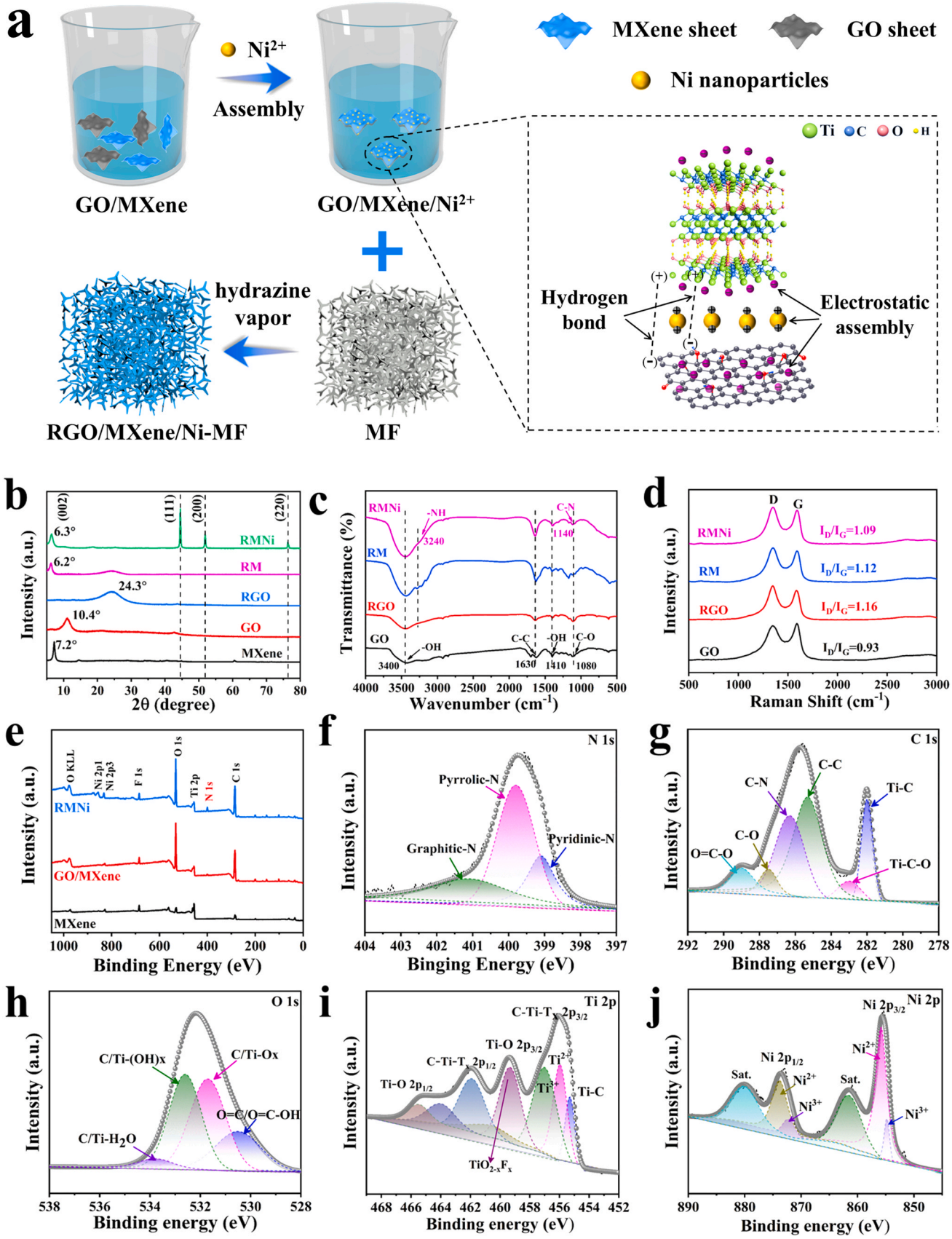

Fig. 1. Preparation and characterization of RGO/MXene/Ni-melamine foam (RMNi-MF). (a) Schematic illustration of fabricating RMNi-MF. (b) The XRD patterns, (c) FT-IR, (d) Raman spectra of MXene, GO, RGO, RGO/MXene and RGO/MXene/Ni hybrid. (e) The XPS spectra of MXene, GO/MXene and RGO/MXene/Ni, (f) N 1s, (g) C 1s, (h) O 1s, (i) Ti 2p, (j) Ni 2p.

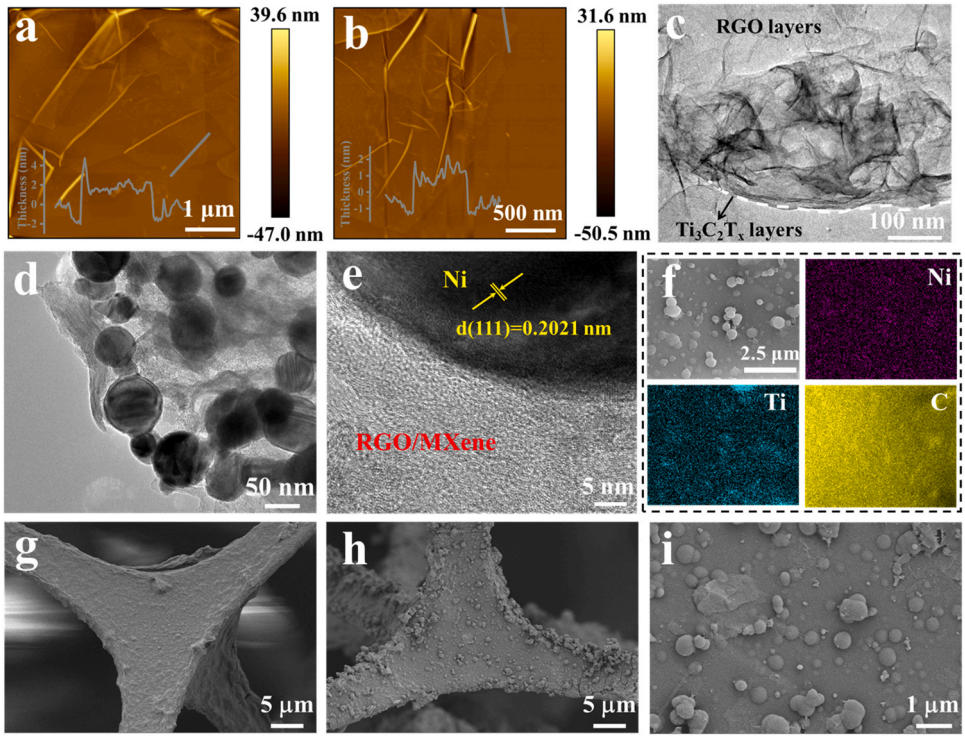

Fig. 2. Morphological Characterization of RMNi-MF. The AFM images of (a) GO and (b) MXene sheet. The TEM images of (c) RGO/MXene sheet hybrids, (d) RGO/MXene/Ni hybrids, (e) HRTEM. The SEM images of (g) RGO/MXene-MF and (h-i) RMNi -MF. (f) The corresponding elemental mapping images of RMNi-MF hybrid.

(Fig. 2b). In addition, GO and MXene can be firmly assembled (Fig. 2c). The TEM images of the RMNi hybrid further demonstrate the interface and crystal structure. Among them, Ni magnetic nanoparticles are uniformly attached to the GO/MXene sheet (Fig. 2d). In addition, the periodically well-defined lattice spacing (~0.2021 nm) was allocated to face-centered cubic (111) Ni crystals, confirming the perfect crystallinity of the anchored Ni magnetic particles (Fig. 2e), which was consistent with the XRD results. The synthesized RGO, RGO/MXene and RMNi hybrids were integrated onto the MF surface by a dip coating process. Unlike the smooth surface of MF (Fig. S1), the framework of RGO/MXene-MF has a large number of curled and wrinkled RGO/MXene sheets were successfully assembled (Fig. 2g). While for RMNi-MF, it can be observed that a great deal of homogeneous and dense Ni magnetic nanoparticles was anchored on the RGO/MXene sheet (Fig. 2h, i), and the RMNi hybrids are firmly packaged and assembled on the MF framework. The Ni, Ti, and C elemental mapping of RMNi hybrids on the MF framework further confirms the homogeneous dispersion of Ni magnetic nanoparticles on the RGO/MXene sheets (Fig. 2f). It is worth noting that the Ni magnetic nanoparticles anchored on the RGO/MXene surface can generate a large number of interfaces through the electrostatic self-assembly process, creating a "micro-capacitor" structure that facilitates improved impedance matching and interfacial polarization. In addition, the 3D conductive/magnetic network formation of the RMNi heterojunction along the MF backbone facilitates more efficient electron transfer and enhances conduction and magnetic losses. The 3D porous structure of MF facilitates the multiple reflections, scattering and absorption of EMW in the absorbing material.

In general, EMW absorption properties are related to electromagnetic parameters. The complex permittivity ($\varepsilon_r = \varepsilon' - j\varepsilon''$) and complex permeability ($\mu_r = \mu' - j\mu''$) are commonly used to evaluate EMW absorption performance. Among them, the real part (ε' and μ') and the imaginary part (ε'' and μ'') represent the storage capacity and dissipation capacity of EMW, respectively [50]. The frequency-dependent electromagnetic parameters of RGO-MF, RGO/MXene-MF, R1M2Ni-MF, R1M1Ni-MF and R2M1Ni-MF are shown in Fig. S2. It can be found that the dielectric constant exhibits a typical decreasing trend over the entire frequency range due to frequency dispersion effects. Among them, the values of ε' and ε'' of RGO-MF are lower, dropping from 5.7 to 3.7 and 1.9 to 1.1 in the 2–18 GHz frequency range, respectively, indicating that RGO-MF's storage and dissipation capacity of electromagnetic energy is not ideal. With the introduction of ultra-high conductivity MXene, RGO/MXene-MF exhibits a higher complex permittivity, and the values of ε' and ε'' drop from 18.9 to 10.9 and 14.9 to 6.7, respectively. After electrostatic self-assembly of Ni magnetic nanoparticles on RGO/MXene sheets, the values of ε' and ε'' of the obtained R1M1Ni-MF are 9.1–4.5 and 6.4–2.3, respectively. Based on the classical free electron theory ($\varepsilon'' \approx 1/2\pi\varepsilon_0\rho f$), the values of ε' and ε'' increase with conductivity [51]. Different from the RGO/MXene-MF, owing to the introduction of numerous non-conductive Ni magnetic nanoparticles and the reduction of RGO/MXene content, electron transport efficiency is effectively reduced, leading to a decline in ε''. Here, the ε' and ε'' values of RMNi-MF could be significantly enhanced by tuning the ratio of GO to MXene. It can be deduced that the homogeneous distribution of Ni magnetic nanoparticles on the RGO/MXene sheets contributes to the enhanced EMW absorption, which might originate from better impedance matching ability.

Generally, the complex permeability was described as: $\mu' = 1 + \frac{M}{H}\cos\theta$ and $\mu'' = 1 + \frac{M}{H}\sin\theta$. where M, H and θ represent the magnetization, the external magnetic field, and the phase lag angle of the magnetization behind the external magnetic field, respectively [52]. In detail, the μ' value of both RGO-MF and RGO/MXene remains around 1.04 and μ'' remains around 0, which can be attributed to the non-magnetic properties of RGO and RGO/MXene. However, owing to the existence of Ni magnetic nanoparticles, the μ' and μ'' values of RMNi-MF are slightly increased. The saturation magnetization values of R1M2Ni-MF, R1M1Ni-MF and R2M1Ni-MF are 11.8 emu/g, 10.7 emu/g and 12.3 emu/g, respectively (Fig. S3a), confirming that Ni magnetic nanoparticles with strong Ms value and weak Hc process improve the magnetic permeability of the composite. Theoretically, magnetic loss is caused by three factors, including natural resonance, exchange

resonance and eddy current loss [53]. Among them, the eddy current effect can be evaluated by the calculated value of C_0: $C_0 = \mu''(\mu')^{-2}f^{-1}$. If only eddy current losses are the dominant factor in the magnetic loss, the value of C_0 should be constant over the entire frequency range [54]. Fig. S3b shows that the C_0 value of RMNi-MF exhibits a fluctuating trend, which indicates the existence of natural resonance and exchange resonance. Among them, the formants in the low-frequency region and the high-frequency region belong to the natural resonance and the exchange resonance, respectively [55].

To further study the electromagnetic loss of the composite foam, the dielectric loss and magnetic loss of RMNI-MF were studied in detail. The calculated dielectric loss tangent ($\tan\varepsilon = \varepsilon''/\varepsilon'$) and magnetic loss tangent ($\tan\mu = \mu''/\mu'$) are shown in Fig. S2c,f. The results show that both RGO/MXene-MF and RMNi-MF foams exhibit higher Tanε values, while RGO-MF has lower Tanε values. Notably, RGO/MXene-MF and RMNi-MF exhibit strong fluctuations at high frequencies, indicating a polarization process. Generally, the polarization process mainly includes conductance loss, interface polarization and dipole polarization [56]. Here, Cole-Cole diagrams are introduced to study relaxation phenomena during polarization. The type of dielectric loss can be depicted by the relationship between ε' and ε'' according to the classical Debye relaxation model. It could be represented by the following equation:

$$\varepsilon' = \varepsilon_\infty + \frac{\varepsilon_s - \varepsilon_\infty}{1 + \omega^2\tau^2} \tag{1}$$

$$\varepsilon'' = \frac{\varepsilon_s - \varepsilon_\infty}{1 + \omega^2\tau^2}\omega\tau + \frac{\sigma}{\omega\varepsilon_0} \tag{2}$$

$$\left(\varepsilon' - \frac{\varepsilon_s + \varepsilon_\infty}{2}\right)^2 + (\varepsilon'')^2 = \left(\frac{\varepsilon_s - \varepsilon_\infty}{2}\right)^2 \tag{3}$$

Where ε_∞ and ε_s stands for the relative permittivity at the high-frequency limit and the static permittivity, ω, τ and σ represent the angular frequency, polarization relaxation and conductivity [57]. The polarization losses (interfacial/dipole polarization) and conduction losses of the EMW passing through the RMNi-MF foam are confirmed by the multiple linear-tailed semicircle curves in Cole as shown in Fig. S4. Specifically, on the one hand, Ni magnetic nanoparticles are anchored on the surface of the RGO/MXene sheet, forming a great number of interfaces, causing interface polarization and enhancing the dielectric loss. In addition, the "micro-capacitor" structure formed by RGO/MXene and Ni nanoparticles results in the accumulation and rearrangement of space charges, which in turn induces the interfacial polarization process. On the other hand, the rich functional groups and defects on the surface of RGO/MXene sheets could create a great amount of dipoles, which could induce dipole polarization and related relaxation processes. The MF skeleton provides a 3D transmission path for electron movement, resulting in conduction loss.

Generally, the EMW absorption performance of syntactic foam is evaluated by calculating the RL value, based on the transmission line theory formula as follows:

$$Z_{in} = Z_0\sqrt{\frac{\mu_r}{\varepsilon_r}}\tanh\left(j\frac{2\pi fd}{c}\sqrt{\mu_r\varepsilon_r}\right) \tag{4}$$

$$RL = 20\log_{10}\left|\frac{Z_{in} - Z_0}{Z_{in} + Z_0}\right| \tag{5}$$

Where Z_{in} is the input impedance of the absorber, Z_0 was the impedance of free space, f is the testing frequency, d represents the thickness, and c is the velocity of light [58]. The RL value of an ideal absorber needs to be lower than − 10 dB, and the EMW exceeding 90% will be attenuated, and the frequency range corresponding to the RL_{min} value lower than − 10 dB is defined as EAB [59]. To illustrate visually the relationship between RL value, thickness and frequency, the 3D reflection losses of RGO-MF, RGO/MXene-MF and RMNi-MF could be seen in Fig. 3(a-e). Meanwhile, the RL value can be adjustable through changing the thickness (Fig. S5). Among them, the RGO-MF syntactic foam exhibits weak EMW absorption performance with an RL_{min} value of − 13.1 dB at 9.2 GHz and a thickness of 4 mm. The high matching thickness and low reflection loss are mainly attributed to poor electrical conductivity. After the introduction of ultra-high conductivity MXene, the absorbing performance of RGO/MXene-MF is still not ideal, the RL_{min} can reach − 18.2 dB, and the EAB is 4.16 GHz, the poor impedance matching and a single loss mechanism limit improvements in absorber performance. Comprehensive electromagnetic parameter analysis, too high or too low

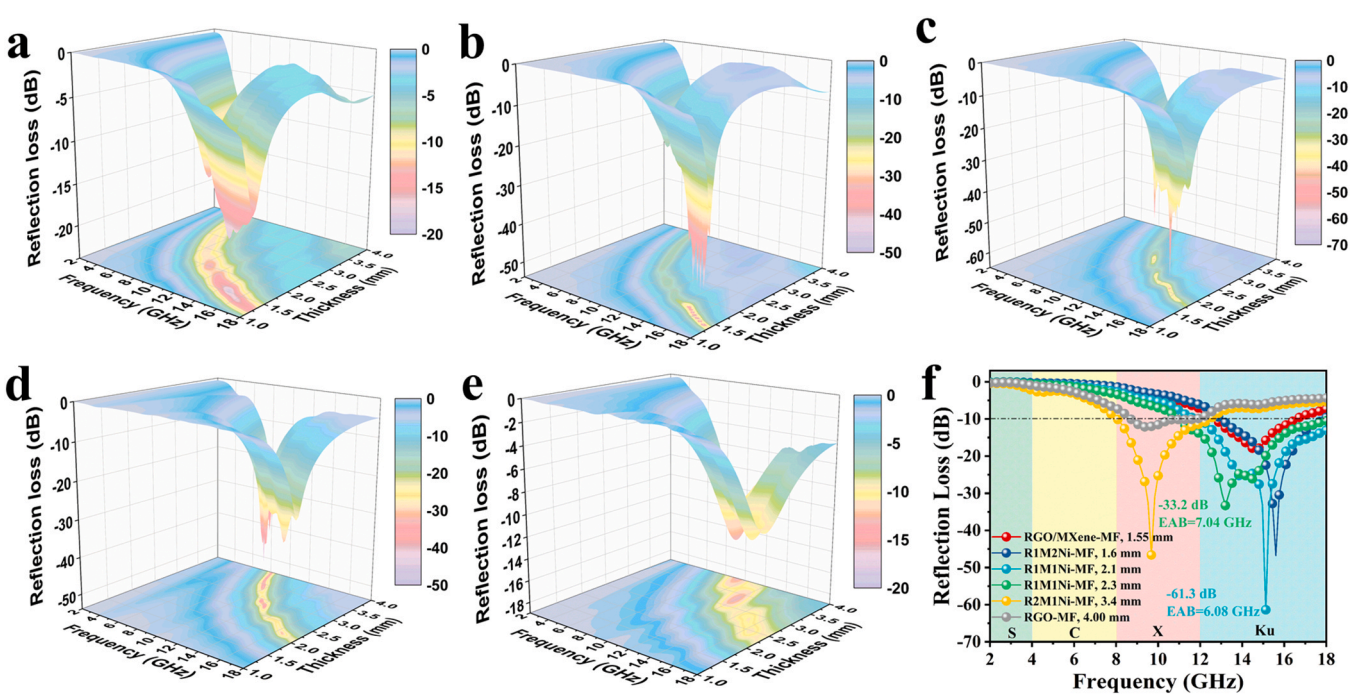

Fig. 3. Microwave absorption properties of RMNi-MF. 3D RL performance of (a) RGO/MXene-MF, (b) R1M2Ni-MF, (c) R1M1Ni-MF, (d) R2M1Ni-MF and (e) RGO-MF as well as (f) 2D RL performance. Among them, R1M1Ni-MF exhibits excellent microwave absorption performance.

dielectric constant is not conducive to obtaining excellent EMW absorption performance. When the Ni magnetic nanoparticles were fully assembled with the RGO/MXene sheets, the R1M1Ni-MF exhibited excellent EMW absorption properties. In particular, at a thickness of 2.1 mm, the RL_{min} value reached − 61.3 dB and EAB of 6.08 GHz. The EAB could reach as high as 7.04 GHz (from 10.96 to 18 GHz) at 2.3 mm (Fig. 3f). In addition, composite foams with different EMW absorption properties were obtained by changing the ratio of RGO to MXene. Among them, the RL_{min} value of R1M2Ni-MF reached − 46.7 dB with a thickness of 1.6 mm, the maximum EAB achieved 5.12 GHz at 2 mm. The R2M1Ni-MF possess an RL value of − 46.6 dB with a thickness of 3.4 mm and a maximum EAB of 6.72 GHz with a thickness of 2.55 mm. Furthermore, as the thickness increases, the peak of the RL curve shifts from high frequency to low frequency, which can be explained by a quarter wavelength (1/4λ) with the following equation:

$$t_m = \frac{n\lambda}{4} = \frac{nc}{4f_m\sqrt{|\varepsilon_r||\mu_r|}}(n = 1, 3, 5, \ldots) \tag{6}$$

The results show that the matched thicknesses of R1M2Ni-MF, R1M1Ni-MF, and R2M1Ni-MF agree with the calculated thicknesses, proving the accuracy of the quarter-wavelength model (Fig. S6). The above results show that the R1M1Ni-MF composite foam has excellent EMW absorption capability and is hopefully a promising material for EMW absorption.

In general, impedance matching and attenuation capabilities were key factors influencing EMW absorption properties [60]. The EMW incident on the surface of the absorbing material is generally reflected, absorbed and transmitted. Optimized impedance matching reduces reflection and increases the absorption of EMW. Here, impedance matching can be evaluated by introducing $|Z_{in}/Z_0|$, which can be calculated according to the following formula:

$$\frac{Z_{in}}{Z_0} = \sqrt{\frac{\mu_r}{\varepsilon_r}}\tanh\left(j\frac{2\pi fd}{c}\sqrt{\mu_r\varepsilon_r}\right) \tag{7}$$

To minimize reflections and encourage numerous EMW to enter the absorber and be attenuated, the value of $|Z_{in}/Z_0|$ should be close to 1 (0.8–1.2) [61]. Fig. 4(a–e) shows 2D contour plots of $|Z_{in}/Z_0|$ values for all samples, values of 0.8 and 1.2 are marked with red lines. Among them, the $|Z_{in}/Z_0|$ value of RGO/MXene-MF is well below 1, and the $|Z_{in}/Z_0|$ value of RGO-MF is well above 1. Due to the impedance mismatch, the EMW shows a lot of reflection in the absorber, and the EMW has poor absorption. In contrast, the red line of RMNi-MF covers a wider range of thickness and frequency, and the range of $|Z_{in}/Z_0|$ value close to 1 of R1M1Ni-MF is the widest, achieving excellent impedance matching. Therefore, impedance matching can be optimized by electromagnetic parameters, which are dependent on the structure and composition of the absorbing material. Here, the electromagnetic parameters are related to the electrical conductivity, Ni magnetic nanoparticles, and porous structure in RMNi-MF composites, respectively. The absorbed EMW are dissipated or converted into heat energy. Here, the attenuation constant (α) is introduced to evaluate the attenuation capability of the absorber, which can be described as:

$$\alpha = \frac{\sqrt{2}}{c}\pi f \times \sqrt{(\mu''\varepsilon'' - \mu'\varepsilon') + \sqrt{(\mu''\varepsilon'' - \mu'\varepsilon')^2 + (\mu'\varepsilon'' + \mu''\varepsilon')^2}} \tag{8}$$

Fig. 4f shows the frequency-dependent attenuation constant α of the composite foam. In particular, the value of α increases in the order of RGO-MF < R2M1Ni-MF < R1M1Ni-MF < R1M2Ni-MF < RGO/MXene-MF, which indicates that RGO/MXene-MF possess the strongest ability to attenuate EMW. However, its microwave absorption performance was not ideal, which indicated that the microwave absorption performance was not completely determined by the dissipation capacity.

To further clarify the potential relationship between impedance matching, attenuation capability and EMW absorption performance, the frequency-dependent $|Z_{in}/Z_0|$, α and RL_{min} values of R1M1Ni-MF are discussed in detail (Fig. 5a). It could be seen that as the frequency increases, α reached a maximum value of 224.5. However, the RL_{min} value is not ideal. In contrast, RL_{min} reaches a minimum value of − 61.3 dB as the value of $|Z_{in}/Z_0|$ approaches 1. The results show that the balance between impedance matching and attenuation capability is beneficial to achieving excellent microwave absorption performance. The EMW absorption properties of the relevant MF matrix composites are listed in

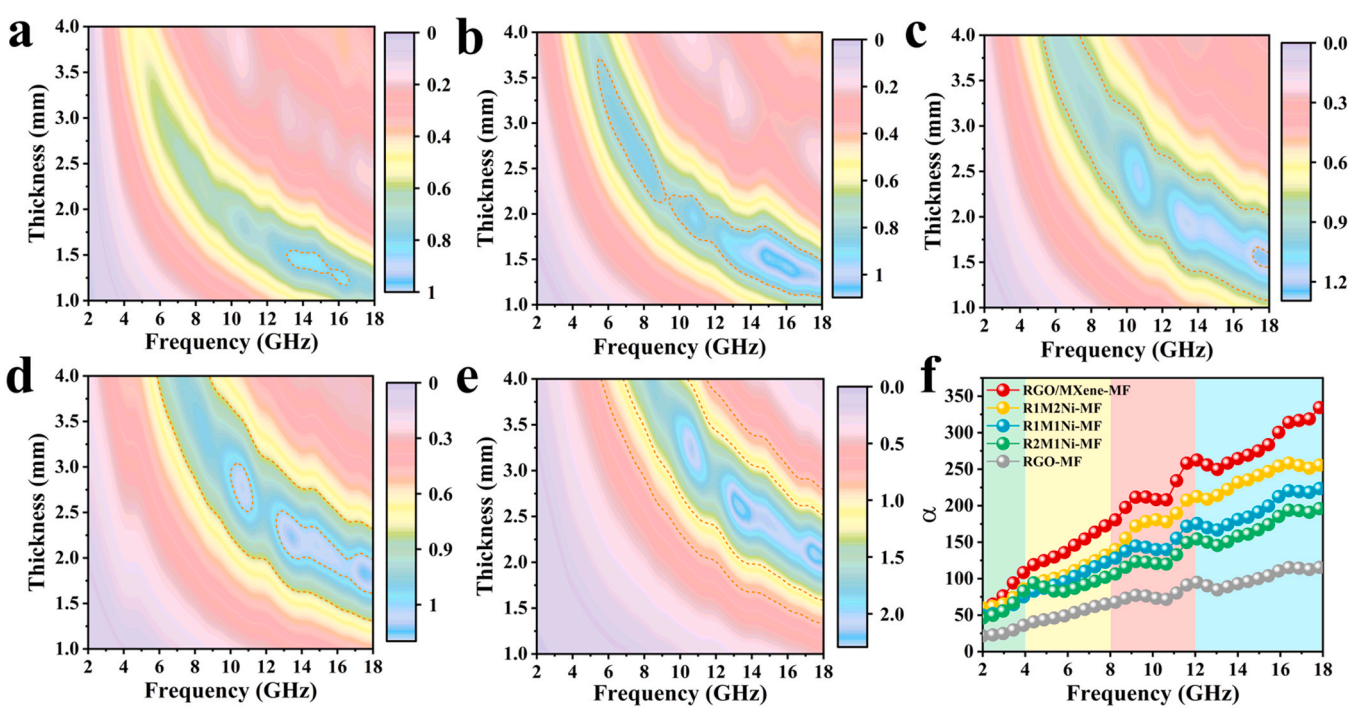

Fig. 4. Impedance matching of RMNi-MF. Impedance matching of (a) RGO/MXene-MF, (b) R1M2Ni-MF, (c) R1M1Ni-MF, (d) R2M1Ni-MF and (e) RGO-MF as well as (f) their attenuation constant. Among them, R1M1Ni-MF show proper impedance matching and excellent microwave attenuation ability.

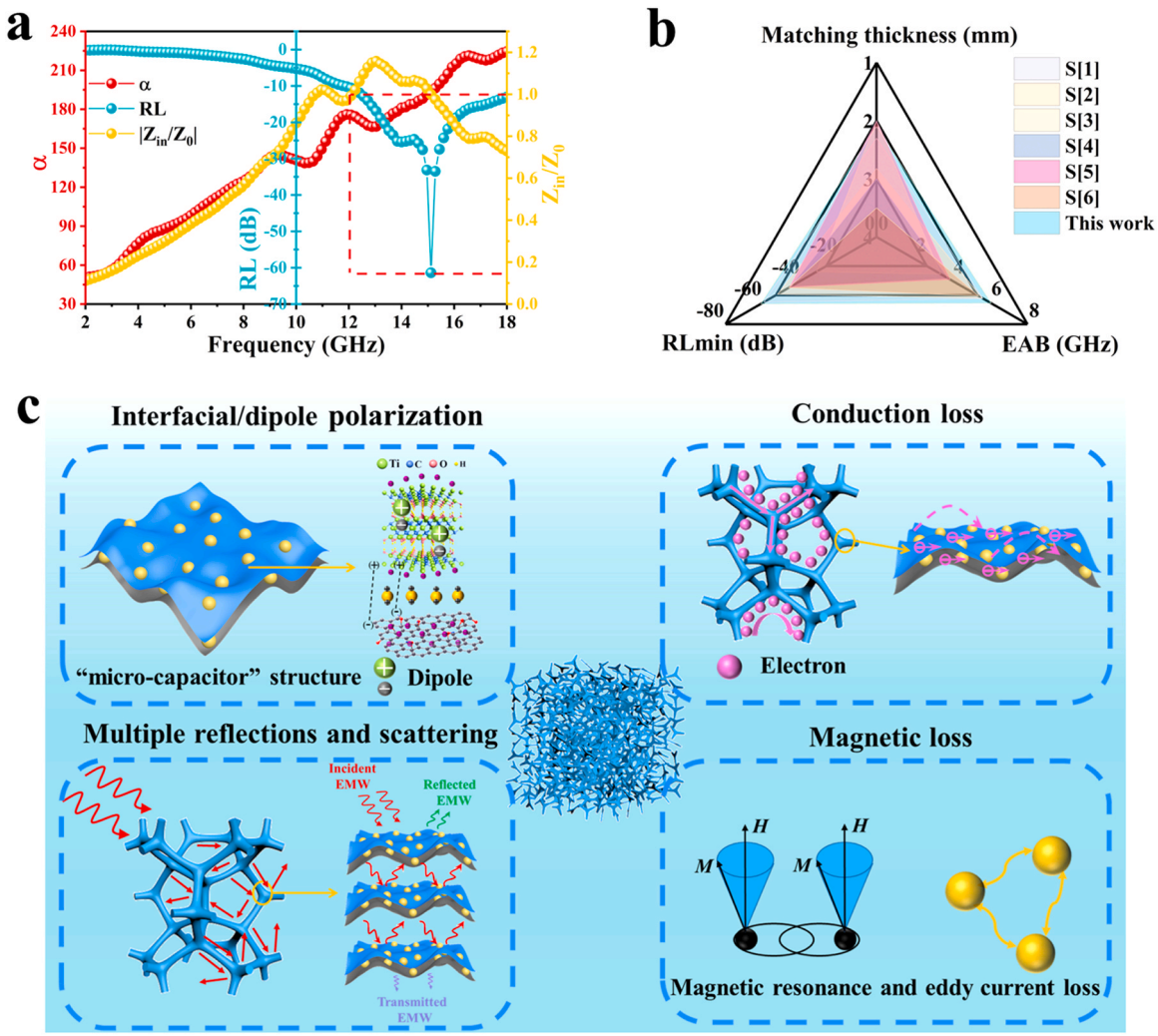

Fig. 5. Microwave absorption mechanism of RMNi-MF. (a) α/RL/Z−f curve of R1M1Ni-MF. (b) Compared with the reported mf based foam composites, R1M1Ni-MF exhibit excellent microwave absorbing properties. (c) Schematic illustration of microwave absorption mechanisms for the RMNi-MF.

Fig. 5b and Table S1. Compared with these materials, R1M1Ni-MF possess the advantages of strong absorption, wide EAB and thin matching thickness, and can be regarded as an ideal material for EMW absorption.

Based on the above discussion, the EMW absorption mechanism of RMNi-MF composites foam was proposed in Fig. 5c. First, the interconnected conductive network provided by the 3D porous structure of RMNi-MF can efficiently transport electrons, thereby causing conduction losses to attenuate incident EMW [62]. On the one hand, the non-conductive Ni magnetic nanoparticles are uniformly grown on the conductive RGO/MXene surface, and the large number of heterogeneous interfaces provided by the formed "micro-capacitor" structure can lead to charge accumulation, resulting in interface polarization loss [63]; On the other hand, the abundant functional groups, intrinsic defects and doped N elements on the surface of RGO/MXene hybrids can induce dipole/defect polarization at high-frequency electromagnetic fields [64]. In addition, the adjacent Ni particles will produce a magnetic coupling effect when interacting with EMW, hindering the transmission of EMW [65]. The Ni particles themselves attenuate EMW energy through exchange resonance and natural resonance under the alternating electromagnetic field [66–68]. Lastly, the 3D porous interconnection network structure contributes to the optimized impedance matching of the material, extending the transmission path of EMW in the foam, which is conducive to multiple reflections and scattering. Meanwhile, EMW is also reflected and scattered among the RGO, MXene and Ni particles.

In order to meet the complex and changeable application environment, high-performance absorbing materials often need to have multiple functions such as heat insulation, infrared stealth performance, hydrophobicity and non-combustibility. Among them, absorbing materials with excellent thermal insulation properties can effectively protect military weapons or electronic devices from high-temperature damage. The R1M1Ni-MF sample with a thickness of about 1 cm was deposited in the centre of a circular heating stage with a set temperature of 80 °C. The infrared thermal imaging images from 5 to 30 min was shown in Fig. 6a, and the surface temperatures of the samples were ~33.5 °C, ~33.9 °C, ~34.1 °C, and ~34.3 °C, respectively. The results show that R1M1Ni-MF possesses excellent thermal insulation properties and can effectively prevent heat transfer. With the increase in heating time, the top surface temperature is stable, indicating that the sample has excellent thermal insulation stability. In addition, the excellent thermal insulation performance endows it with infrared stealth to achieve the purpose of hiding military targets. Generally, the higher the surface temperature of an object, the stronger the intensity of infrared radiation. As shown in Fig. 6b,c, under the infrared camera, the colour of the bare hand is different from its surroundings. On the contrary, when the R1M1Ni-MF is placed on the hand, the colour of the coverage area is consistent with the surrounding, making it disappear under the infrared detection device, realizing the infrared stealth function. Through the finite element simulation and thermal insulation mechanism analysis in

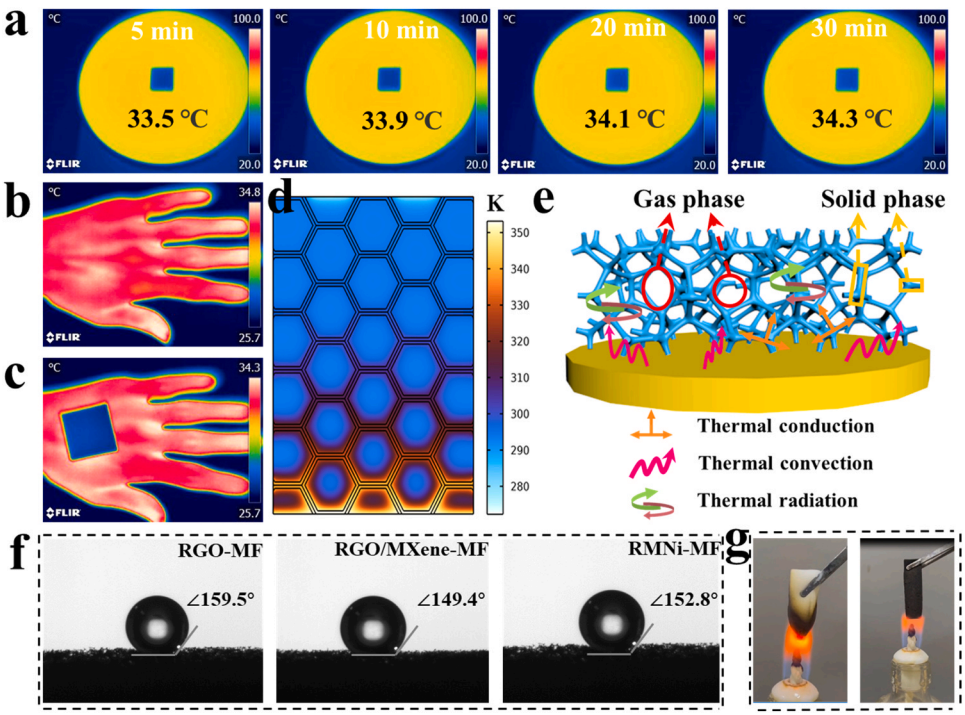

Fig. 6. The application of RMNi-MF in complex environments. Thermal infrared images of RMNi-MF(2 *2 *1 cm) captured (a) on a heating stage with a temperature of 80 °C at different time, and (b, c) on the hand, showing the excellent thermal insulation properties. (d) Finite element simulation of the temperature change in the RGO/MXene/Ni-MF. (e) The schematic diagram of the heat transfer mechanism of RMNi-MF. (f) Water contact angle images of RGO-MF, RGO/MXene and RMNi-MF with good hydrophobicity. (g) Flame retardant experiment of MF and RMNi-MF.

the foam (Fig. 6d, e), it can be found that a substantial quantity of air in the R1M1Ni-MF composite foam can reduce the radiant heat transfer capacity of the solid phase. Furthermore, the reduced/modified syntactic foam showed excellent hydrophobicity with WCAs of 159.5°, 149.4° and 152.8° for RGO-MF, RGO/MXene-MF and R1M1Ni-MF, respectively (Fig. 6f). When exposed to the environment, the hydrophobicity of composite foams endows them waterproof, corrosion-resistant and ice-resistant. In addition, the incombustibility of R1M1Ni-MF was evaluated by combustion experiments in the air. The inherent flame retardancy of MF makes it possible to form a dense coke layer on the surface of the combustion body after contacting an open flame to retard the combustion, with no smoke, no droplets, and self-extinguishing from the fire, but the shape has changed. On the contrary, the shape of R1M1Ni-MF does not change after combustion, which is due to the dense flame-retardant protective layer formed via the RGO/MXene/Ni hybrid assembled on the MF, while the high porosity can promote rapid heat diffusion during the combustion process (Fig. 6g and Movie S1–2). In summary, the R1M1Ni-MF syntactic foam exhibits excellent high-performance EMW absorption, thermal insulation, infrared stealth, hydrophobicity, and non-flammability.

Supplementary material related to this article can be found online at doi:10.1016/j.nantod.2023.101958.

Conclusion

In summary, multifunctional RMNi-MF composite foams were successfully fabricated by electrostatic self-assembly, dip-coating adsorption, and hydrazine vapor reduction. The appropriate multi-component strategy and ingenious structural design endow the R1M1Ni-MF with excellent impedance matching and strong attenuation capability, achieving excellent EMW absorption performance with a RL_{min} as high as − 61.3 dB (2.1 mm) and an EAB maximum of 7.04 GHz (2.3 mm). This is attributed to strong conduction loss, abundant interfacial polarization, dipole polarization, multiple reflection scattering and synergistic electromagnetic loss effects. In addition, the excellent multifunctionality of thermal insulation, infrared shielding, hydrophobicity and non-combustibility endows the R1M1Ni-MF composite foam with application potential in various environments. Therefore, this work provides a new design idea for the development of multifunctional syntactic foams with high-performance EMW absorption.

Experimental Section

Materials

Graphite (300 mesh), potassium permanganate ($KMnO_4$), hydrochloric acid (HCl, 37%), sodium nitrate ($NaNO_3$), nickel chloride hexahydrate ($NiCl_2{\cdot}6\,H_2O$), ethylene glycol (EG), ethanol, hydroxide Sodium (NaOH), hydrazine hydrate ($N_2H_4{\cdot}H_2O$, 80%), Dopamine hydrochloride and Tris were purchased from Sinopharm Chemical Reagent Co., Ltd. (China). Ti_3AlC_2 MAX phase (400 mesh) was provided by 11 Technology Co., Ltd. (China). Lithium fluoride (LiF) was obtained from Aladdin Reagent Co. Ltd. The GO used in this work was synthesized by a modified Hummers method.

Synthesis of $Ti_3C_2T_x$ MXene

$Ti_3C_2T_x$ MXenes are prepared by etching the Al layer in the Ti_3AlC_2 MAX phase. First, 40 ml HCl and 2 g LiF powder were added to a 100 ml Teflon container and stir for 20 min. Then, 2 g Ti_3AlC_2 powder was slowly added to the mixed solution and continued stirring for 24 h in an oil bath at 35 °C. The resulting mixture was then centrifuged and washed three times in distilled water until the pH was 6. Subsequently, few-layer $Ti_3C_2T_x$ MXene nanosheets were obtained by adding ethanol and ultrasonication. Finally, the unexfoliated $Ti_3C_2T_x$ was removed by centrifugation, and the dark green upper dispersion was collected and freeze-dried to obtain $Ti_3C_2T_x$ MXene nanosheets.

Fabrication of GO/MXene/Ni-MF Hybrids

In a typical procedure, a homogeneous GO/MXene suspension could be obtained by simply suspending a proportion of GO and MXene nanosheets in a solution of 35 ml EG and 15 ml H_2O followed by sonication for 20 min. Then, a stoichiometric $NiCl_2{\cdot}6\,H_2O$ was added and stirred for 20 min (GO/MXene: Ni^{2+}, the mass ratio of 1:2). The PDA-modified MF foams were then dipped into the GO/MXene/Ni^{2+}

suspension, and the resulting GO/MXene/Ni^{2+}-MF was reduced through treatment with hydrazine hydrate at 90 °C for 10 h. Finally, RGO/MXene/Ni-MF (RMNi-MF) was obtained, in which the RGO/MXene/Ni (RMNi) hybrid was also prepared by the same procedure. Depending on the different mass ratios of GO and MXene (x:y), the acquired RMNi-MF were named RxMyNi-MF, respectively.

Characterization

The microscopic morphology and structure were observed using atomic force microscopy (AFM, Bruker MultiMode 8), transmission electron microscopy (TEM, FEI Tecnai G2 F20) and scanning electron microscopy (SEM, Zeiss Sigma 300). The crystal structure was identified through XRD (Bruker D8 Advance XRD) with Cu Kα radiation (λ = 0.154 nm). The chemistry structure was characterized via FTIR (FT-IR, Nicolet 6700), Raman spectroscopic system (Horiba LabRAM HR Evolution) spectrometers, and XPS (Thermo Scientific ESCALAB 250Xi). The magnetic property was measured via a vibrating sample magnetometer (VSM, 7404, LakeShore). The infrared radiation intensity measurement using infrared cameras (FLIR E60). The water contact angle was measured through an optical contact angle measurement system. The coaxial method was used to measure the EM parameters. The obtained samples were completely Immersed in liquid paraffin in a vacuum oven at 80 °C until the pores of the sample are filled with paraffin. After cooling and solidifying, the samples were cut into concentric rings (ϕin = 3.04 mm, ϕout = 7.00 mm) for measurement.

CRediT authorship contribution statement

Haoran Cheng: Methodology, Data curation, Writing – original draft. **Yamin Pan:** Investigation, Writing – review & editing. **Wei Li:** Formal analysis. **Chuntai Liu:** Supervision, Funding acquisition. **Changyu Shen:** Resources, Funding acquisition. **Xianhu Liu:** Conceptualization, Methodology, Validation, Formal analysis, Investigation, Writing – review & editing, Supervision, Project administration. **Caofeng Pan:** Methodology, Validation, Writing – review & editing.

Declaration of Competing Interest

The authors declare that they have no known competing financial interests or personal relationships that could have appeared to influence the work reported in this paper.

Data Availability

Data will be made available on request.

Acknowledgements

The authors thank the National Key R&D Program of China (2019YFA0706802) for financial support. The authors would like to thank Gang Li from shiyanjia Lab (www.shiyanjia.com) for test of XPS and TEM.

Appendix A. Supporting information

Supplementary data associated with this article can be found in the online version at doi:10.1016/j.nantod.2023.101958.

References

[1] A. Iqbal, F. Shahzad, K. Hantanasirisakul, M.K. Kim, J. Kwon, J. Hong, H. Kim, D. Kim, Y. Gogotsi, C.M. Koo, Anomalous absorption of electromagnetic waves by 2D transition metal carbonitride Ti_3CNT_x (MXene), Science 369 (2020) 446–450.
[2] Y. Zhang, X. Wang, M. Cao, Confinedly implanted $NiFe_2O_4$-rGO: cluster tailoring and highly tunable electromagnetic properties for selective-frequency microwave absorption, Nano Res 11 (2018) 1426–1436.
[3] R.C. Che, L.M. Peng, X.F. Duan, Q. Chen, X.L. Liang, Microwave absorption enhancement and complex permittivity and permeability of Fe encapsulated within carbon nanotubes, Adv. Mater. 16 (2004) 401–405.
[4] H. Sun, R. Che, X. You, Y. Jiang, Z. Yang, J. Deng, L. Qiu, H. Peng, Cross-stacking aligned carbon-nanotube films to tune microwave absorption frequencies and increase absorption intensities, Adv. Mater. 26 (2014) 8120–8125.
[5] H. Cheng, Y. Pan, X. Wang, C. Liu, C. Shen, D.W. Schubert, Z. Guo, X. Liu, Ni Flower/MXene-melamine foam derived 3D magnetic/conductive networks for ultra-efficient microwave absorption and infrared stealth, Nano-Micro Lett. 14 (2022) 1–16.
[6] M.S. Cao, Y.Z. Cai, P. He, J.C. Shu, W.Q. Cao, J. Yuan, 2D MXenes: electromagnetic property for microwave absorption and electromagnetic interference shielding, Chem. Eng. J. 359 (2019) 1265–1302.
[7] Y. Zhang, Y. Huang, T. Zhang, H. Chang, P. Xiao, H. Chen, Z. Huang, Y. Chen, Broadband and tunable high-performance microwave absorption of an ultralight and highly compressible graphene foam, Adv. Mater. 27 (2015) 2049–2053.
[8] A. Iqbal, P. Sambyal, C.M. Koo, 2D MXenes for electromagnetic shielding: a review, Adv. Funct. Mater. 30 (2020) 2000883.
[9] J. Cheng, L. Cai, Y. Shi, F. Pan, Y. Dong, X. Zhu, H. Jiang, X. Zhang, Z. Xiang, W. Lu, Polarization loss-enhanced honeycomb-like MoS_2 nanoflowers/undaria pinnatifida-derived porous carbon composites with high-efficient electromagnetic wave absorption, Chem. Eng. J. 431 (2022), 134284.
[10] J. Wang, Z. Wu, Y. Xing, L. Liu, A novel 1D/2D interpenetrating network architecture of MXene/cellulose composite microfiber and graphene for broadband microwave absorption, Chem. Eng. J. 439 (2022), 135734.
[11] Z. Wu, H.W. Cheng, C. Jin, B. Yang, C. Xu, K. Pei, H. Zhang, Z. Yang, R. Che, Dimensional design and core–shell engineering of nanomaterials for electromagnetic wave absorption, Adv. Mater. 34 (2022) 2107538.
[12] R. Shu, Z. Wan, J. Zhang, Y. Wu, Y. Liu, J. Shi, M. Zheng, Facile design of three-dimensional nitrogen-doped reduced graphene oxide/multi-walled carbon nanotube composite foams as lightweight and highly efficient microwave absorbers, ACS Appl. Mater. Interfaces 12 (2019) 4689–4698.
[13] X. Li, C. Wen, L. Yang, R. Zhang, X. Li, Y. Li, R. Che, MXene/FeCo films with distinct and tunable electromagnetic wave absorption by morphology control and magnetic anisotropy, Carbon 175 (2021) 509–518.
[14] Y. Zhang, M.K. Xu, Z. Wang, T. Zhao, L.X. Liu, H.B. Zhang, Z.Z. Yu, Strong and conductive reduced graphene oxide-MXene porous films for efficient electromagnetic interference shielding, Nano Res (2022) 1–9.
[15] S. Zhao, H.B. Zhang, J.Q. Luo, Q.W. Wang, B. Xu, S. Hong, Z.Z. Yu, Highly electrically conductive three-dimensional $Ti_3C_2T_x$ MXene/reduced graphene oxide hybrid aerogels with excellent electromagnetic interference shielding performances, ACS Nano 12 (2018) 11193–11202.
[16] Q. Song, F. Ye, L. Kong, Q. Shen, L. Han, L. Feng, G. Yu, Y. Pan, H. Li, Graphene and MXene nanomaterials: toward high-performance electromagnetic wave absorption in gigahertz band range, Adv. Funct. Mater. 30 (2020) 2000475.
[17] Z. Lin, J. Liu, W. Peng, Y. Zhu, Y. Zhao, K. Jiang, M. Peng, Y. Tan, Highly stable 3D $Ti_3C_2T_x$ MXene-based foam architectures toward high-performance terahertz radiation shielding, ACS Nano 14 (2020) 2109–2117.
[18] X. Li, X. Yin, C. Song, M. Han, H. Xu, W. Duan, L. Cheng, L. Zhang, Self-assembly core–shell graphene-bridged hollow MXenes spheres 3D foam with ultrahigh specific EM absorption performance, Adv. Funct. Mater. 28 (2018) 1803938.
[19] L. Liang, Q. Li, X. Yan, Y. Feng, Y. Wang, H. Zhang, X. Zhou, C. Liu, C. Shen, X. Xie, Multifunctional magnetic $Ti_3C_2T_x$ MXene/Graphene aerogel with superior electromagnetic wave absorption performance, ACS Nano 15 (2021) 6622–6632.
[20] X. Li, Z. Wu, W. You, L. Yang, R. Che, Self-assembly MXene-rGO/CoNi film with massive continuous heterointerfaces and enhanced magnetic coupling for superior microwave absorber, Nano-Micro Lett. 14 (2022) 1–14.
[21] P. Yi, Z. Yao, J. Zhou, B. Wei, L. Lei, R. Tan, H. Fan, Facile synthesis of 3D Ni@C nanocomposites derived from two kinds of petal-like Ni-based MOFs towards lightweight and efficient microwave absorbers, Nanoscale 13 (2021) 3119–3135.
[22] J. Tao, J. Zhou, Z. Yao, Z. Jiao, B. Wei, R. Tan, Z. Li, Multi-shell hollow porous carbon nanoparticles with excellent microwave absorption properties, Carbon 172 (2021) 542–555.
[23] J. Wang, L. Liu, S. Jiao, K. Ma, J. Lv, J. Yang, Hierarchical carbon fiber@MXene@MoS2 core-sheath synergistic microstructure for tunable and efficient microwave absorption, Adv. Funct. Mater. 30 (2020) 2002595.
[24] X. Yan, X. Huang, Y. Chen, Y. Liu, L. Xia, T. Zhang, H. Lin, D. Jia, B. Zhong, G. Wen, A theoretical strategy of pure carbon materials for lightweight and excellent absorption performance, Carbon 174 (2021) 662–672.
[25] H.Y. Wang, X. b Sun, G.S. Wang, A MXene-modulated 3D crosslinking network of hierarchical flower-like MOF derivatives towards ultra-efficient microwave absorption properties, J. Mater. Chem. A 9 (2021) 24571–24581.
[26] C. Wen, X. Li, R. Zhang, C. Xu, W. You, Z. Liu, B. Zhao, R. Che, High-density anisotropy magnetism enhanced microwave absorption performance in $Ti_3C_2T_x$ MXene@Ni microspheres, ACS Nano 16 (2021) 1150–1159.
[27] J. Yang, J. Wang, H. Li, Z. Wu, Y. Xing, Y. Chen, L. Liu, MoS_2/MXene aerogel with conformal heterogeneous interfaces tailored by atomic layer deposition for tunable microwave absorption, Adv. Sci. 9 (2022) 2101988.
[28] X. Zhu, Y. Dong, Z. Xiang, L. Cai, F. Pan, X. Zhang, Z. Shi, W. Lu, Morphology-controllable synthesis of polyurethane-derived highly cross-linked 3D networks for multifunctional and efficient electromagnetic wave absorption, Carbon 182 (2021) 254–262.
[29] Y. Shi, X. Ding, K. Pan, Z. Gao, J. Du, J. Qiu, A novel multi-dimensional structure of graphene-decorated composite foam for excellent stealth performance in microwave and infrared frequency bands, J. Mater. Chem. A 10 (2022) 7705–7717.

[30] W. Gu, J. Tan, J. Chen, Z. Zhang, Y. Zhao, J. Yu, G. Ji, Multifunctional bulk hybrid foam for infrared stealth, thermal insulation, and microwave absorption, ACS Appl. Mater. Interfaces 12 (2020) 28727–28737.
[31] K. Su, Y. Wang, K. Hu, X. Fang, J. Yao, Q. Li, J. Yang, Ultralight and high-strength SiCnw@SiC foam with highly efficient microwave absorption and heat insulation properties, ACS Appl. Mater. Interfaces 13 (2021) 22017–22030.
[32] J. Yan, Y. Huang, C. Chen, X. Liu, H. Liu, The 3D CoNi alloy particles embedded in N-doped porous carbon foams for high-performance microwave absorbers, Carbon 152 (2019) 545–555.
[33] K.L. Zhang, J.Y. Zhang, Z.L. Hou, S. Bi, Q.L. Zhao, Multifunctional broadband microwave absorption of flexible graphene composites, Carbon 141 (2019) 608–617.
[34] F. Pan, L. Cai, Y. Shi, Y. Dong, X. Zhu, J. Cheng, H. Jiang, X. Wang, Y. Jiang, W. Lu, Heterointerface engineering of β-Chitin/Carbon Nano-Onions/Ni-P composites with boosted maxwell-wagner-sillars effect for highly efficient electromagnetic wave response and thermal management, Nano-Micro Lett. 14 (2022) 1–18.
[35] Y. Li, X. Liu, X. Nie, W. Yang, Y. Wang, R. Yu, J. Shui, Multifunctional organic–inorganic hybrid aerogel for self-cleaning, heat-insulating, and highly efficient microwave absorbing material, Adv. Funct. Mater. 29 (2019) 1807624.
[36] Y. Dong, X. Zhu, F. Pan, Z. Xiang, X. Zhang, L. Cai, W. Lu, Fire-retardant and thermal insulating honeycomb-like NiS2/SnS_2 nanosheets@ 3D porous carbon hybrids for high-efficiency electromagnetic wave absorption, Chem. Eng. J. 426 (2021), 131272.
[37] H.G. Shi, H.B. Zhao, B.W. Liu, Y.Z. Wang, Multifunctional flame-retardant melamine-based hybrid foam for infrared stealth, thermal insulation, and electromagnetic interference shielding, ACS Appl. Mater. Interfaces 13 (2021) 26505–26514.
[38] Y. Ma, Y. Yue, H. Zhang, F. Cheng, W. Zhao, J. Rao, S. Luo, J. Wang, X. Jiang, Z. Liu, 3D synergistical MXene/reduced graphene oxide aerogel for a piezoresistive sensor, ACS Nano 12 (2018) 3209–3216.
[39] L. Liang, R. Yang, G. Han, Y. Feng, B. Zhao, R. Zhang, Y. Wang, C. Liu, Enhanced electromagnetic wave-absorbing performance of magnetic nanoparticles-anchored 2D $Ti_3C_2T_x$ MXene, ACS Appl. Mater. Interfaces 12 (2019) 2644–2654.
[40] B. Zhao, X. Guo, W. Zhao, J. Deng, B. Fan, G. Shao, Z. Bai, R. Zhang, Facile synthesis of yolk–shell Ni@void@SnO_2(Ni_3Sn_2) ternary composites via galvanic replacement/Kirkendall effect and their enhanced microwave absorption properties, Nano Res 10 (2016) 331–343.
[41] X. Li, W. You, L. Wang, J. Liu, Z. Wu, K. Pei, Y. Li, R. Che, Self-assembly-magnetized MXene avoid dual-agglomeration with enhanced interfaces for strong microwave absorption through a tunable electromagnetic property, ACS Appl. Mater. Interfaces 11 (2019) 44536–44544.
[42] D. Lai, X. Chen, Y. Wang, Controllable fabrication of elastomeric and porous graphene films with superior foldable behavior and excellent electromagnetic interference shielding performance, Carbon 158 (2020) 728–737.
[43] Y. Zhou, X. Deng, H. Xing, H. Zhao, Y. Liu, L. Guo, J. Feng, W. Feng, Y. Zong, X. Zhu, Dynamically observing the formation of MOFs-driven Co/N-doped carbon nanocomposites by in-situ transmission electron microscope and their application as high-efficient microwave absorbent, Nano Res (2022) 1–12.
[44] J. Liu, H.B. Zhang, R. Sun, Y. Liu, Z. Liu, A. Zhou, Z.Z. Yu, Hydrophobic, flexible, and lightweight mxene foams for high-performance electromagnetic-interference shielding, Adv. Mater. 29 (2017) 1702367.
[45] O. Mashtalir, M. Naguib, V.N. Mochalin, Y. Dall Agnese, M. Heon, M.W. Barsoum, Y. Gogotsi, Intercalation and delamination of layered carbides and carbonitrides, Nat. Commun. 4 (1) (2013) 7.
[46] P. He, M.S. Cao, J.C. Shu, Y.Z. Cai, X.X. Wang, Q.L. Zhao, J. Yuan, Atomic layer tailoring titanium carbide MXene to tune transport and polarization for utilization of electromagnetic energy beyond solar and chemical energy, ACS Appl. Mater. Interfaces 11 (2019) 12535–12543.
[47] A. Sheng, Y. Yang, D.X. Yan, K. Dai, H. Duan, G. Zhao, Y. Liu, Z.M. Li, Self-assembled reduced graphene oxide/nickel nanofibers with hierarchical core-shell structure for enhanced electromagnetic wave absorption, Carbon 167 (2020) 530–540.
[48] J. Wang, F. Wu, Y. Cui, A. Zhang, Q. Zhang, B. Zhang, Efficient synthesis of N-doped porous carbon nanoribbon composites with selective microwave absorption performance in common wavebands, Carbon 175 (2021) 164–175.
[49] J. Yan, Y. Huang, X. Han, X. Gao, P. Liu, Metal organic framework (ZIF-67)-derived hollow CoS_2/N-doped carbon nanotube composites for extraordinary electromagnetic wave absorption, Compos. Pt. B-Eng. 163 (2019) 67–76.
[50] Z. Xiang, X. Zhu, Y. Dong, X. Zhang, Y. Shi, W. Lu, Enhanced electromagnetic wave absorption of magnetic Co nanoparticles/CNTs/EG porous composites with waterproof, flame-retardant and thermal management functions, J. Mater. Chem. A 9 (2021) 17538–17552.
[51] R. Zhang, L. Wang, C. Xu, C. Liang, X. Liu, X. Zhang, R. Che, Vortex tuning magnetization configurations in porous Fe_3O_4 nanotube with wide microwave absorption frequency, Nano Res (2022) 1–8.
[52] Z. Xiang, X. Zhang, Y. Shi, L. Cai, J. Cheng, H. Jiang, X. Zhu, Y. Dong, W. Lu, Efficient microwave absorption of MOFs derived laminated porous Ni@C nanocomposites with waterproof and infrared shielding versatility, Carbon 185 (2021) 477–490.
[53] W. You, K. Pei, L. Yang, X. Li, X. Shi, X. Yu, H. Guo, R. Che, In situ dynamics response mechanism of the tunable length-diameter ratio nanochains for excellent microwave absorber, Nano Res 13 (2019) 72–78.
[54] S. ur Rehman, J. Wang, Q. Luo, M. Sun, L. Jiang, Q. Han, J. Liu, H. Bi, Starfish-like C/$CoNiO_2$ heterostructure derived from ZIF-67 with tunable microwave absorption properties, Chem. Eng. J. 373 (2019) 122–130.
[55] X.X. Wang, T. Ma, J.C. Shu, M.S. Cao, Confinedly tailoring Fe_3O_4 clusters-NG to tune electromagnetic parameters and microwave absorption with broadened bandwidth, Chem. Eng. J. 332 (2018) 321–330.
[56] T. Hou, B. Wang, M. Ma, A. Feng, Z. Huang, Y. Zhang, Z. Jia, G. Tan, H. Cao, G. Wu, Preparation of two-dimensional titanium carbide ($Ti_3C_2T_x$) and $NiCo_2O_4$ composites to achieve excellent microwave absorption properties, Compos. Pt. B-Eng. 180 (2020), 107577.
[57] X. Zhang, J. Qiao, J. Zhao, D. Xu, F. Wang, C. Liu, Y. Jiang, L. Wu, P. Cui, L. Lv, High-efficiency electromagnetic wave absorption of cobalt-decorated NH_2-UIO-66-derived porous ZrO_2/C, ACS Appl. Mater. Interfaces 11 (2019) 35959–35968.
[58] F. Pan, L. Cai, Y. Shi, Y. Dong, X. Zhu, J. Cheng, H. Jiang, X. Wang, S. Zhong, W. Lu, Phase engineering reinforced multiple loss network in apple tree-like liquid metal/Ni-Ni_3P/N-doped carbon fiber composites for high-performance microwave absorption, Chem. Eng. J. 435 (2022), 135009.
[59] B. Deng, Z. Liu, F. Pan, Z. Xiang, X. Zhang, W. Lu, Electrostatically self-assembled two-dimensional magnetized MXene/hollow Fe_3O_4 nanoparticle hybrids with high electromagnetic absorption performance and improved impendence matching, J. Mater. Chem. A 9 (2021) 3500–3510.
[60] X. Xu, G. Wang, G. Wan, S. Shi, C. Hao, Y. Tang, G. Wang, Magnetic Ni/graphene connected with conductive carbon nano-onions or nanotubes by atomic layer deposition for lightweight and low-frequency microwave absorption, Chem. Eng. J. 382 (2020), 122980.
[61] B. Zhao, G. Shao, B. Fan, W. Zhao, Y. Xie, R. Zhang, Synthesis of flower-like CuS hollow microspheres based on nanoflakes self-assembly and their microwave absorption properties, J. Mater. Chem. A 3 (2015) 10345–10352.
[62] B. Zhao, Y. Li, Q. Zeng, L. Wang, J. Ding, R. Zhang, R. Che, Galvanic replacement reaction involving core–shell magnetic chains and orientation-tunable microwave absorption properties, Small 16 (2020) 2003502.
[63] P. Liu, Z. Yao, J. Zhou, Z. Yang, L.B. Kong, Small magnetic Co-doped NiZn ferrite/graphene nanocomposites and their dual-region microwave absorption performance, J. Mater. Chem. C. 4 (2016) 9738–9749.
[64] Y. Cui, K. Yang, J. Wang, T. Shah, Q. Zhang, B. Zhang, Preparation of pleated RGO/MXene/Fe_3O_4 microsphere and its absorption properties for electromagnetic wave, Carbon 172 (2021) 1–14.
[65] Y. Qiu, Y. Lin, H. Yang, L. Wang, M. Wang, B. Wen, Hollow Ni/C microspheres derived from Ni-metal organic framework for electromagnetic wave absorption, Chem. Eng. J. 383 (2020), 123207.
[66] Q. Liu, Q. Cao, H. Bi, C. Liang, K. Yuan, W. She, Y. Yang, R. Che, CoNi@SiO_2@TiO_2 and CoNi@Air@TiO_2 microspheres with strong wideband microwave absorption, Adv. Mater. 28 (2016) 486–490.
[67] R. Che, C. Zhi, C. Liang, X. Zhou, Fabrication and microwave absorption of carbon nanotubes/ $CoFe_2O_4$ spinel nanocomposite, Appl. Phys. Lett. 88 (2006), 033105.
[68] Z. Wu, K. Pei, L. Xing, X. Yu, W. You, R. Che, Enhanced microwave absorption performance from magnetic coupling of magnetic nanoparticles suspended within hierarchically tubular composite, Adv. Funct. Mater. 29 (2019) 1901448.

Haoran Cheng received his MSc degree from Zhengzhou University. Since 2020, he has been a PhD candidate under the supervision of Prof. Changyu Shen and Prof. Xianhu Liu at the National Engineering Research Center for Advanced Polymer Processing Technology, Zhengzhou University. His research field is developing functional polymer materials and exploring their applications in electromagnetic interference shielding and microwave absorption.

Xianhu Liu is currently a professor at the National Engineering Research Center for Advanced Polymer Processing Technology, Zhengzhou University, China. In 2016, he received his PhD degree from Friedrich-Alexander-University Erlangen-Nuremberg, Germany (2016). His research focuses on polymer processing in functional applications.

Caofeng Pan received his BS degree (2005) and PhD degree (2010) in materials science and engineering from Tsinghua University, China. He then joined the group of Prof. Zhong Lin Wang at Georgia Institute of Technology as a postdoctoral fellow from 2010 to 2013. He is currently a professor and a group leader at Beijing Institute of Nanoenergy and Nanosystems, Chinese Academy of Sciences. His research interests mainly focus on the fields of piezotronics/piezophototronics for fabricating new electronic and optoelectronic devices, nanopower source, hybrid nanogenerators, and self-powered nanosystems. Details can be found at http://www.piezotronics.cn/.